Wind and Structures, *Vol. 22, No. 2 (2016) 161-184*
DOI: http://dx.doi.org/10.12989/was.2016.22.2.161

Aerodynamic characteristics investigation of Megane multi-box bridge deck by CFD-LES simulations and experimental tests

Elena Dragomirescu*, Zhida Wang[a] and Michael S. Hoftyzer[b]

Department of Civil Engineering, University of Ottawa, 161 Louis Pasteur, Ottawa, K1N 6N5, ON, Canada

(Received March 15, 2015, Revised October 30, 2015, Accepted December 4, 2015)

Abstract. Long-span suspension bridges have evolved through the years and with them, the bridge girder decks improved as well, changing their shapes from standard box-deck girders to twin box and multi-box decks sections. The aerodynamic characteristics of the new generation of twin and multiple-decks are investigated nowadays, to provide the best design wind speeds and the optimum dimensions such bridges could achieve. The multi-box Megane bridge deck is one of the new generation bridge decks, consisting of two side decks for traffic lanes and two middle decks for railways, linked between them with connecting beams. Three-dimensional CFD simulations were performed by employing the Large Eddy Simulation (LES) algorithm with a standard Smagorinsky subgrid-scale model, for $Re = 9.3 \times 10^7$ and angles of attack α = -4°, -2°, 0°, 2° and 4°. Also, a wind tunnel experiment was performed for a scaled model, 1:80 of the Megane bridge deck section, for $Re = 5.1 \times 10^5$ and the aerodynamic static coefficients were found to be in good agreement with the results obtained from the CFD-LES model. However the aerodynamic coefficients determined individually, from the CFD-LES model, for each of the traffic and railway decks of the Megane bridge, varied significantly, especially for the downstream traffic deck. Also the pressure distribution and the effect of the spacing between the connecting beams, on the wind speed profiles showed a slight increase in turbulence above the downstream traffic and railway decks.

Keywords: multi-box Megane bridge deck; aerodynamic coefficients; CFD simulation; wind tunnel experiments; wind flow patterns

1. Introduction

A tendency of improving the bridge aerodynamics through optimizing the geometrical configurations of the bridge deck shape has been noticed, for long-span suspension and cable-stayed bridges, departing entirely from the I-beam girder deck, used for the design of the initial Tacoma Bridge, which collapsed in 1940. Due to the progress in understanding the aerodynamic phenomena, and the mechanisms of the flow-structure interaction, stability of long-span bridges has greatly improved (Wardlaw 1992, Larsen *et al.* 1995, Matsumoto *et al.* 2007, Caracoglia 2011, etc.). New bridge deck geometries, adopting several slots between the decks which are connected by stabilizing beams, can work efficiently for extending the span lengths of

*Corresponding author, Professor, E-mail: elndrag@uottawa.ca
[a] M.A.Sc. Student, E-mail: zwang112@uottawa.ca
[b] Ph.D. Student, E-mail: mhoft084@uottawa.ca

http://www.techno-press.org/?journal=was&subpage=8 ISSN: 1226-6116 (Print), 1598-6225 (Online)

these bridges. The bluff-body characteristics of the twin-box and multi-box decks configurations confer a better aerodynamic performance, which is an important aspect when designing super-long span bridges (Ostenfeld and Larsen 1992, Morita *et al.* 1995, Ge *et al.* 2008, Chen *et al.* 2013). The significant increase of span length for suspension bridges, implies an increase of weight for the box and truss decks, therefore in order to maintain the separation ratio within the range characterizing the aerodynamic stability of these types of decks, the torsional frequency must be increased, and this is generally achieved by adopting a higher depth of the box deck section (Larsen *et al.* 2000, Ge and Xiang 2009). Several initiatives of designing multi-box decks have been considered for super long-span bridges, such as Messina Bridge (Diana *et al.* 1995), Gibraltar Strait Bridge (Lin and Chow 1991), Sunda Strait Bridge (Wangsadinata *et al.* 1992), while construction of twin box deck bridges has been already blooming in recent years: Stonecutters Bridge (Hui *et al.* 2008), Tsing Ma Bridge (Xu *et al.* 1997), Xihoumen Bridge (Ge and Xiang 2009), Yi Sun-Sin Bridge (Lee *at al.* 2014), Gwangyang Bridge (Park *et al.* 2009), etc.

Shaping individually three or four box decks separated by slots and connecting them at equal intervals by stabilizing beams, thus forming an active wind flow circulation system between the decks, has proved to lower the values of the torsional frequency, up to values for which the aerodynamic stability condition would be satisfied (Brown 1999). Also, another advantage of using the twin-box and multi-box girder decks is that by slotting the deck, the difference of pressure between the top and bottom girders is reduced, and sometimes no additional countermeasures for aerodynamic instabilities are required (Larsen *et al.* 1995). For a single-box bridge deck however, besides the relatively higher deck height which must be considered in order to increase the torsional frequency of the deck and due to the compact shape, as aerodynamic countermeasure, stabilizing plates must be often installed at both deck edges (Larsen 2008).

One of the first and most comprehensive experimental studies investigating different slot patterns and fairings configurations for slotted box girders of 0% to 47% slot ratios (slot width to girder width ratio) was carried out by Sato *et al.* (1995), who found out that using one slot (corresponding to 20% slot ratio) in the middle of the box deck, two smaller slots opened near the edges of the deck (corresponding to 20% slot ratio), and the combination of one slot in the middle and two slots near the edge of the deck (corresponding to 40% slot ratio), would considerably lower the on-set flutter velocity for a deck with fairings, when compared with a conventional full box girder. When the number of slots and the girder width were increased, the same study (Sato *et al.* 1995) showed that the flutter velocity increased, the highest values of 68 m/s and 64 m/s being recorded for the girder deck with a large slot in the middle and two smaller slots near the edges (33 % slot ratio), and for a girder deck of similar configuration, but with additional slots introduced between the deck and the fairings (47% slot ratio), respectively. More recently, the position and the width of the slots for a rectangular deck of aspect ratio B/D = 20 were discussed by Trein *et al.* (2013) and he pointed out that the gaps have a strong impact on the unsteady pressure characteristics of the downstream box, even though a low aerodynamic effect on the model as a whole was noticed. A twin-box bridge deck model, resembling two inverted airfoils, was tested in smooth flow, at $Re = 4.4 \times 10^5$ by Kwok *et al.* (2012) who indicated that, the width of the gap did not have significant effect on the lift force and pitching moment coefficients, however it almost doubled the drag force coefficient for the decks separation exceeding b/B = 16%, where b was the gap width and B was the total width of the twin box deck model. Numerous other studies have investigated the effect of the *Re* number on the scaled section models 1:30, 1:10, 1:80, (Matsuda *et al.* 2001), the flutter performance (Ge and Xiang 2009) or have reported field measurements for vortex-induced vibrations (Li *et al.* 2011), however only a limited number of studies have focused on clarifying the wind flow-structure interaction for twin-box bridge deck configurations (Chen *et al.* 2013, Larsen *et al.* 1988, Larsen and Walther 1997).

Similarly for the multi-box bridge decks, numerous studies were performed for the cross-section proposed for Messina Bridge (Diana *et al.* 2012, Diana *et al.* 2008, Diana *et al.* 1995, Larose *et al.* 1997), which has three interconnected box decks. Most of the investigations focused on the flutter verification, aerodynamic coefficients and efficiency of various aerodynamic countermeasures, but did not detail the wind flow formations through the gaps and around the multiple decks. The flutter instability for Messina multi-box deck experiments occurred beyond the design wind speed of 62 m/s and the reported static aerodynamic coefficients showed a better evolution than most of the conventional full-box girders and twin-box girder decks (Diana *et al.* 2012, Diana *et al.* 1995).

1.1 Geometrical description of the Megane multi-box bridge deck

A multi-box deck section, entitled Megane bridge deck with two side decks for traffic lanes (decks A and D), two middle railway decks (decks B and C), and a total of 3 gaps separating them, was investigated through a three-dimensional CFD simulation, for verifying the static aerodynamic forces and wind flow-structure interaction. The prototype of the Megane multi-box deck has a total width of 62.0 m and a height of 5.0 m; each traffic deck has 16.0 m width and a maximum height of 3.0 m, while the railway decks have 10.0 m width and 2.0 m height (Fig. 1). The gaps between the decks are 3.6 m each and connecting beams of 3.0 m width and 5.0 m height were considered every 10.0 m along the deck. For validating the results of the CFD modelling, a wind tunnel test was performed for a scaled 1:80 section model of the Megane multi-box deck, thus the length of the sectional model tested was 1.0 m and the total width was 0.775 m. The width of the traffic decks A and B was 0.2 m, the width of the railway decks C and D was 0.125 m, while the gaps were 0.045 m and 0.035 m wide, respectively; the maximum height of the model was 0.065 m. The Reynolds number, defined as the ratio of the inertial force to the viscous force of the wind flow (Simiu and Scanlan 1996), should preserve the equality for the prototypes and their models, regardless the geometrical scale in use. In general, it is assumed that very high *Re* numbers do not have a significant effect on the aerodynamic static coefficients, and the Re similarity between the real bridge and the model is often neglected (Larose and D'Auteuil 2008), thus the experimental tests on scaled models are conducted in the range of $Re = 1.0 \times 10^3$ to 1.0×10^4, while the prototype would register *Re* numbers higher than 5.0×10^5. However, several studies have already acknowledged the existence of the *Re* number effect upon the aerodynamic force coefficients for bluff bodies with sharp corners and edges (Schewe 2001, Larose and D'Auteuil 2008) or for bridge deck models (Larose *et al.* 2003, Matsuda *et al.* 2001, Schewe and Larsen 1998, Kwok *et al.* 2012). In order to avoid the potential impact caused by scaling the *Re* number, in the current study a very high scale of 1:2 was employed for the CFD simulation of the multi-box Megane deck model, such that the dimensions of the traffic decks A and D were 8.0 m width and 1.5 m height, for the railway decks B and C were 5.0 m width and 1.0 height and the total width of the deck was 31.0 m. Also the scale of 1:2 was used instead of the full-scale in order to ensure a very small cell dimension at the surface of the model, of 2 mm each, when the refined mesh at the model surface was defined.

For twin or multi-box deck sections, the *Re* number can be calculated based on the chord length of each individual deck, as Larsen *et al.* (2008) recommended when investigating the effect of guiding vanes in mitigating the vortex induced phenomena for the Stonecutters Bridge, or *Re* could be determined using the total width of the deck, from which the gap(s) total width is subtracted (Kuroda *et al.* 1997). The Reynolds number determined for the Megane multi-box bridge deck section was considered as per Eq. (1) below (ASCE 1986), in order to enable the comparison of the currently obtained results with the experimental outcomes from similar bridges deck sections investigations available in the vast literature.

$$Re = \frac{V_p D_p}{\nu} = \frac{V_m D_m}{\nu} \tag{1}$$

where ν is the kinematic viscosity, V_p and V_m are the wind speeds for the prototype and for the model respectively and D_p and D_m are the deck overall widths for the prototype and the model, respectively. Thus the *Re* number for the Megane bridge deck prototype, as illustrated in Fig. 1, was $Re = 6.15 \times 10^8$ and for the Megane bridge deck model used for the three-dimensional CFD simulations was $Re = 9.3 \times 10^7$. Because of the large geometric scale which could be employed for the CFD model of 1:2, the *Re* from the three-dimensional simulations and the *Re* for the prototype differed just by a factor of 6.6, considering also a reduced wind speed of $U_r = 7.26$. For the wind tunnel test however, the Megane bridge deck model, had the scale of 1:80, and the Re numbers were up to $Re = 5.1 \times 10^5$, for the same reduced wind speed. The reduced wind speed is a non-dimensional parameter which normalizes the wind tunnel wind speed, with the natural frequency and the width of the model, as described by Scanlan and Tomoko, (1971)

$$U_r = \frac{\bar{U}}{B \cdot f} \tag{2}$$

where $\bar{U}$ is the mean wind speed, B is the width of the bridge deck and f is the natural frequency of vibration, which was measured for the Megane bridge deck section as 1.67 Hz.

2. CFD simulations and Megane multi-box deck model validation

Given the complex geometry of the Megane multi-box deck section, detailed investigations were performed employing three-dimensional CFD – LES simulations, through the use of Ansys Fluent commercial software.

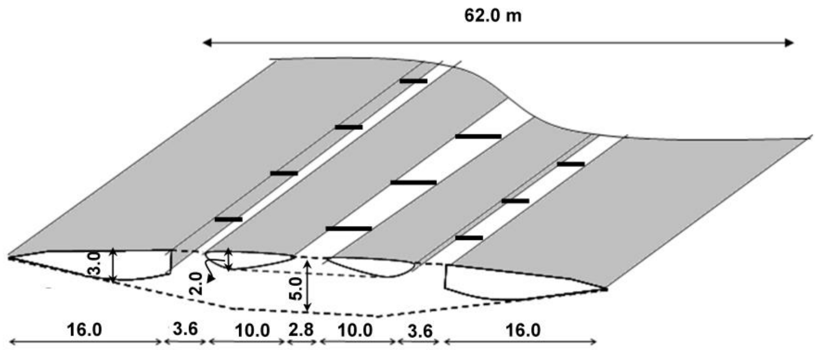

Fig. 1 Geometric dimensions of the Megane multi-box bridge deck section (m)

The current CFD study was performed as a preliminary investigation before finalizing the dimensions and geometry of the Megane multi-box deck to be used for the dynamic wind tunnel tests and flutter instability verification. To validate the results of the LES model, the Unsteady Reynolds Average Navier-Stokes (URANS) algorithm was used, and also a static wind tunnel test was carried out to determine the drag and lift coefficients for the proposed Megane multi-box deck. Once the aerodynamic force coefficients were validated the flow patterns and pressure distributions for the Megane deck section were discussed, based on the LES model. Thus the results from the experimental test were complemented by the outcomes of the CFD simulations.

2.1 Computational domain and mesh details

The rectangular computational domain had the major axis of 5L, the minor axes were L and 1.5 L, where B is the total width of the deck of 31.0 m and L is the length of the deck segment of 20.0 m, as schematically represented in Fig. 2. The non-slip boundary condition was specified on the surfaces of the deck model, and the in-flow boundary condition was set to $u_x = 50$ m/s, $u_y = u_z = 0$, as the incoming wind speed was considered along the x direction. The pressure outlet boundary condition was selected with a cell surface average pressure which allows for pressure variation, while the averaged values do not exceed a static gauge pressure, thus diminishing the reflectivity of the boundary which might be encountered as a reversed flow when coarse meshes are used on the respective boundary. The lateral walls of the domain were considered as symmetric slip with penetration boundary conditions, so that flow can pass through, and the end effect at the extremities of the deck model is avoided. The dimensions of the currently employed simulation domain were relatively smaller than those reported in similar CFD studies (Bruno *et al.* 2014, Nieto *et al.* 2008, Larsen *et al.* 2008, etc.) mostly due to the computer capacity limitations. Considering however the study of Bruno *et al*. (2014) who collected and discussed 70 simulation cases, out of which 51% were LES contributions, 30% were DES contributions and 29% were URANS cases, it was noticed that for a total number of mesh cells n_c varying between 10^5 to 10^7, the span wise grid resolution varied from $\delta z = 1/24$ for coarse grids to $\delta z = 1/100$ in refined grids for simulation domain dimensions between Dx/B=8 to 200, Dy/B=3 to 200 and Dz/B=0.2 to 4, where Dx, Dy, Dz were the length, height and width of the computational domain, while B was the width of the model. The smallest domain reported had dimensions of Dx/B=8, Dy/B = 3 and Dz/B = 0.2 to 1.0, simulation cases reported by Wei and Kareem, 2011, for which it was acknowledged that the flow will be significantly affected, and it was found that the time averaged drag coefficients were higher (C_D = 1.165-1.305) than the other CFD - LES studies (C_D = 0.96-1.04). Lift and pressure coefficients were also found to be higher for the shorter domain used by Wei and Kareem (2011), however for a very high mesh cell number of $n_c = 4.5 \times 10^7$ the pressure coefficient results showed better agreement with other CFD URANS models. The geometry investigated by Bruno *et al.* (2014) represents a basic rectangular cylinder, while the Megane deck has a complex geometry, thus additional studies for complex geometries should also be taken into account. The CFD steady-state RANS study carried out by Blocken and Toparlar (2015) reported pressure and drag reduction results, very similar with the wind tunnel tests, performed on a complicated geometry of a cyclist followed by a car with total length of B = 7.793 m with a space of 1.0 m between them. The simulation domain had a total length of 33.45 m, a width of 16.80 m and a height of 9.45 m, corresponding to 4.29B, 2.15B and 1.21B. The study also proposed a nomogram of potential time reduction as a function of the spacing between the cyclist and the car, as a consequence of drag reduction effect.

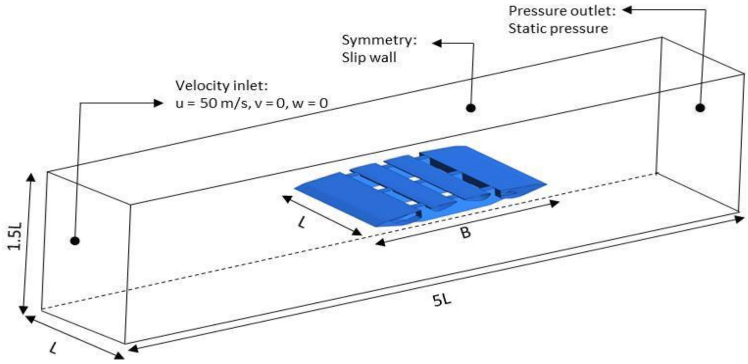

Fig. 2 Geometric details of the computational domain and the Megane bridge deck representation

A grid sensitivity study was performed for the composite geometry of the Megane bridge deck, for 0° angle of attack, varying also the longitudinal dimension of the computational domain. Determining the optimum number and density of the grid nodes is important for obtaining the flow characteristics which should be properly resolved around the multiple-decks of the model. The grid density was increased starting from the Megane model, and expanding towards the limits of the domain. The average drag force was monitored for the bridge deck model for each simulation which ran for 1,000 non-dimensional time steps, or until the drag force converged. A two-dimensional and a three-dimensional domains of dimensions 1L to 10L and 1L to 6L respectively, were created and the drag force convergence steps were compared in Figs. 3(a) and 3(b). The force measured on the Megane bridge deck varied initially, however it achieved a converged value for denser meshes of 53×10^2 nodes for the two-dimensional domain and of 6.24×10^3 nodes for the three-dimensional domain (Fig. 3(a)). Also when different domain sizes were investigated it was noticed that the drag force converged to a specific value for a domain length of 3L for the two-dimensional cases and 5L for the three-dimensional simulations, as it can be noticed in Fig. 3(b). Three-dimensional simulations were performed for lengths up to 6L for angle of attack of 0°, however for -4° and -2° the computation failed to initiate due to computer capacity limitations.

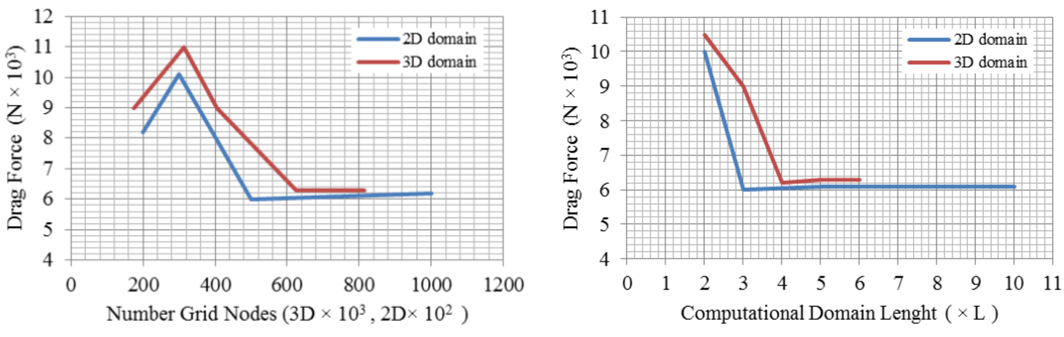

Fig. 3 Drag force convergence with the (a) Number of grid nodes and (b) Domain length

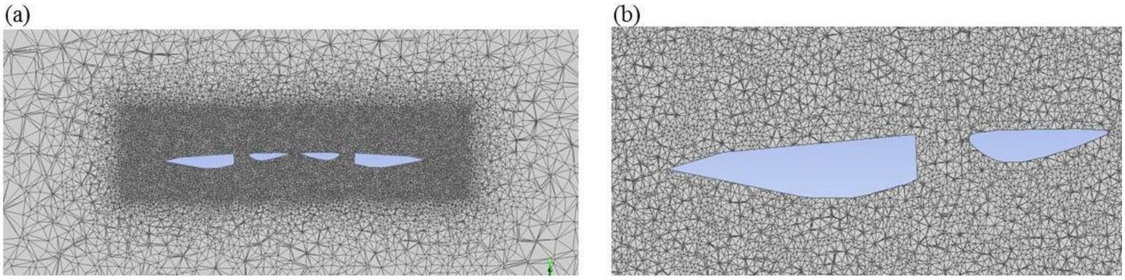

Fig. 4 Three-dimensional mesh in the cross-sectional plane between the beams (a) Computational domain and (b) Megane bridge deck detail

Finally based on the mesh types tested, the optimum mesh choice considered for the current three-dimensional simulation carried out for the Megane bridge deck geometry was the structured tetrahedral mesh, counting for a total number of 3.62×10^6 cells for the entire domain, with 6.24×10^3 nodes, 7.22×10^6 triangular interior faces, 3.3×10^6 faces along the domain's walls. Around the bridge model a very fine mesh was employed with a total of 1.3×10^6 cells (Fig. 4(b)) and 1.5×10^6 triangular faces at the surface of the bridge model. Angles of attack of α = -4°, -2° 0°, 2° and 4° were achieved by changing the orientation of the Megane deck model and re-meshing the domain, preserving as much as possible the mesh parameters expressed above.

Aerodynamic drag and lift coefficients were recorded, and pressure was monitored along the surface of the entire deck segment, on several rings around the decks A, B, C, D and also on several rings around the connecting beams. Velocity profiles were established at the middle of each deck for a height of up to 10 m, and the flow streamlines and pressure distribution were determined for the wind field domain in the immediate vicinity of the deck.

2.2 Turbulent flow algorithms employed for the CFD three-dimensional simulations

The complex geometry of the Megane multi-box deck section complicates the wind-structure interaction phenomena, therefore detailed investigations were performed employing three-dimensional CFD simulations, through the use of Fluent-Ansys commercial software. Two turbulent models, URANS (Unsteady Reynolds Average Navier-Stokes) and LES (Large Eddy Simulation), were initially considered and the most accurate one was retained for further simulations. For both cases the incoming flow conditions were employed as per the smooth flow condition with wind speed constant throughout the incoming wind plane.

The RANS algorithm, first proposed by Osborne Reynolds in 1895 (Osborne 1985) is based on time-averaged Navier-Stokes equations for fluid flow. The basic concept behind this method is the composition of the instantaneous turbulent flow quantity into its time-average quantity and an extra fluctuating component. This calculates directly the average large-scale flow only and the effect brought by the flow turbulence to the average wind speed flow is reflected into the fluctuation part also known as the Reynolds stress. Therefore the required computational costs are greatly reduced. Two main approaches are generally used in conjunction with RANS algorithms: the Reynolds stress model and the eddy viscosity model (Anderson *et al.* 1995). The Reynolds stress model (RSM) is based on satisfying the Reynolds stress equation, with

u_i' and u_j', as dependent variables in the partial differential equations to be solved. However, introducing the transport equations for the Reynolds stresses in all the domain nodes, leads to high computational costs. This model is based on the idea of the molecular viscosity and it was proposed by Boussinesq (Anderson *et al.* 1995). The Reynolds stress tensor is expressed as

$$-u_i u_j = v_T S_{ij} - \frac{2}{3} k \delta_{ij} \tag{3}$$

Here $k = \frac{1}{2}\overline{u_i' u_j'}$ is the turbulent kinetic energy and v_T is the viscosity coefficient and $S_{ij} = \frac{1}{2}\left(\frac{\partial U_i}{\partial x_j} + \frac{\partial U_j}{\partial x_i}\right)$ is the strain-rate tensor and this represents the first proposed eddy viscosity model, which assumes that the relationship between the average speed of the Reynolds stress and the strain rate is linear. Once the average speed strain rate is determined, the six Reynolds stresses need only one viscosity coefficient to be fully identified. The disadvantages lay with the fact that for the cases of unsteady flows and large separated flows, the RANS works with the averaged equations. However, a model was proposed to take into account the unsteadiness within the RANS model, such that the time averaged part of the velocity field is not constant in time and thus its time derivative would lead to a no null value (URANS model). For the current case, the unsteady RANS model was used because the motion of the eddies is considered unsteady and of three-dimensional nature, even when the flow is steady. Thus the eddy viscosity results are more comparable with the results obtained from the LES model.

The LES algorithm considers that the turbulent flow is composed of numerous eddies of different sizes; however only the large-scale eddies would have significant influence on the mean flow, which is fundamentally different from the RANS approach. Thus the LES decomposes the turbulent flow into large-scale and small-scale flow formations by applying a filter at the sub-gird scale model (Smagorisnky 1963). Only the large scale turbulent flow is retained around the structure and it is solved by directly numerical simulations. The Navier-Stokes equations are averaged in the domain delimited by the filter, to remove the small-scale eddies. The filtering process in the LES is most commonly achieved through the Deardorff cassette (BOX) filtering functions, the Fourier filtering functions or the truncated Gaussian filter function. The SGS (subgrid scale) models which have been adopted for LES simulation are the standard Smagorinsky model, Dynamic Smagorinsky model, dynamic hybrid model and gradient model. Among them, the Smagorinsky-Lilly model is the most widely used algorithm. It was proposed in 1963 by Smagorinsky (Smagorisnky 1963) and he also defined the eddy viscosity coefficient as

$$v_T = (C_S \Delta)^2 |\bar{S}| \tag{4}$$

Where $|\bar{S}| = (2\overline{S_{ij} S_{ij}})^{1/2}$ is the rate-of-strain tensor, Δ is the filter scale and C_S is dimensional parameter called Smagorinsky coefficient. The advantage of LES is that this model is able to describe the small-scale turbulent flow and also the computational cost is much smaller than the direct numerical simulations (DNS). The boundary geometry and the flow category have less impact on the SGS stress model when compared to the Reynolds stress model and its application is more universal. Unavoidably, high-speed numerical processing capability is required for processing large amounts of data and solving nonlinear partial differential equations. For the Megane multi-deck bride deck simulation experiment, the Large Eddy Simulation (LES) with the Smagorinsky subgrid-scale model were employed for the CFD simulation. The three-dimensional incompressible Navier-Stokes equation and the equation of continuity in non-dimensional form were used, with Δ as the filter width given as the cubic-root of grid volume and the Smagorinsky constant, C_s = 0.1 to reduce the SGS dissipation, especially if laminar-turbulent flow transition is encountered. A Dynamic Smagorisnky model was not employed herewith, because of its wider width of the filter (approx. 2Δ) when compared with the Smagorinsky model, which in this case would not lead to better results, because of the coarser mesh deployed throughout the computation domain, even if the mesh around the model had very high resolution. The inviscid flux vector was determined by a standard upwind, flux-difference splitting through the low diffusion Roe approach. For estimation of the secondary diffusion terms and velocity derivatives, the least square cell based spatial discretization was employed and Third-Order MUSCL equation was considered for the flow density-based solver. The time step was chosen as Δ_t= 0.0003 s; pressures along the entire surface of the model were integrated, and lift and drag aerodynamic forces were determined.

2.2 LES vs URANS simulations results

The turbulent flows formed around the bridge deck have a direct effect on the drag and lift forces induced by wind to the entire deck. Therefore an accurate estimation, especially when CFD analytical simulations are employed is very important. The URANS and LES numerical algorithms were used in the current investigation both employed for *Re* numbers of $Re = 9.3 \times 10^7$ and angle of attack of 0°. The URANS which considers the Re stresses when calculating the fluctuating wind speed component in the governing equations, has showed more uniform eddy viscosity distribution around the decks A, B, C and D indicating a consistent turbulent flow formation downstream each deck (Fig. 5(a)). The LES however, which filters out the smaller eddies and numerically solves the large scale eddies formed around the structure provided more detailed information regarding the eddy viscosity showing the development of the turbulent flow not only at the edge of the deck, but shortly downstream each deck as well (Fig. 5(b)).

The magnitudes of the eddy viscosities reported in Figs. 5(a) and 5(b) are different because the two models interpret differently this parameter. The LES eddy viscosity is determined for the sub-grid scale eddies around the deck, thus much smaller than the eddy viscosity determined from the Re stress tensor in URANS, which is based on the nonlinear term of the Navier-Stokes equations. In the LES model, which are using on the implicit filtering approach, the eddy viscosity is obtained from the more complex SGS stress tensor. The mixing length is employed through the Smagorinsky model which uses the grid spacing as the length which should be in the inertial range of the turbulent spectrum. In URANS the mixing length is not related to the resolution of the grid but is somehow larger as it has to represent a different range of flow scales.

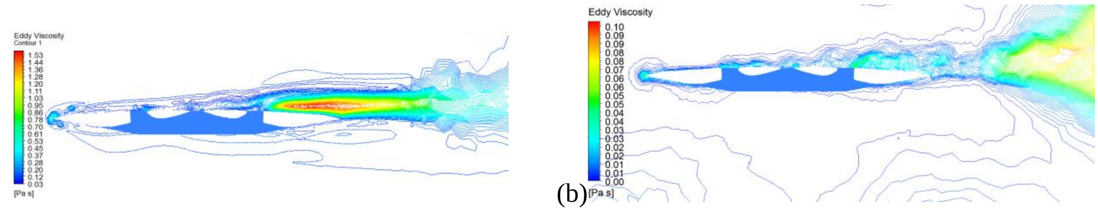

(a) (b)

Fig. 5 Eddy viscosity distribution around the Megane deck for 50 m/s for (a) URANS and (b) LES

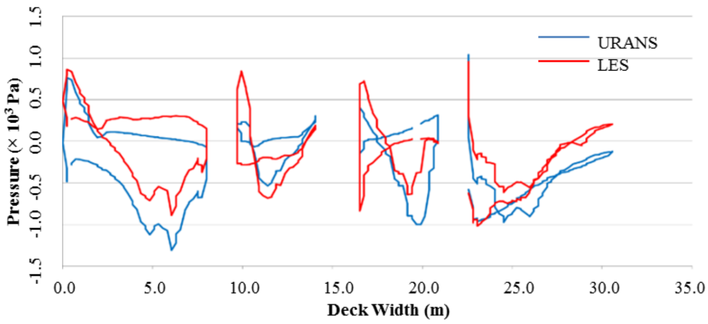

Fig. 6 Instant pressure distribution around each deck with LES and URANS model

Therefore the subgrid viscosity in LES is significantly smaller than the eddy viscosity in URANS. The magnitude of the eddy viscosities from the LES and URANS have different values, however by comparing the instantaneous pressure distribution around the circumference of the individual decks of the Megane section for the same instance at the end of the 1,000 non-dimensional steps of the simulations can provide more information regarding the results agreement. Thus it was noticed that the URANS model tended to underestimate the pressure for the first two decks, which were exposed the most to wind flow variation, when comparing to the LES pressure results. Also for the middle decks B and C, URANS estimated slightly lower wind-induced pressures than the LES method, while the windward edge of deck B has a spike of positive pressure which does not occur when URANS is used (Fig. 6). Therefore the LES method was considered more appropriate for the current CFD simulation because the Megane bridge deck section has multiple decks situated close to each other; hence the wake from the upstream decks will always influence the downstream decks.

The pressure coefficients averaged over the 1,000 non-dimensional time steps of each simulation were determined for the entire Megane bridge deck model, as an average of the upper deck surface, dominated by positive pressures and the lower deck surface, where mostly suction was registered. The mean pressure coefficients $Cp_{URANS} = 0.55$ and $Cp_{LES} = 0.8$ show that even if the eddy viscosity is higher for the URANS model, the overall pressure induced by the flow to the deck model can be higher.

3. Wind flow patterns around the Megane multi-box bridge deck

As also pointed out by other researchers (Larsen *et al.* 2008, Chen *et al.* 2013) for a twin-box deck section, the decks individually immersed in the wind flow, might encounter vortex shedding phenomena for lower *Re*, while for higher *Re* the wind flow would change to a turbulent regime and shear layers will be generated. Larsen *et al.* (2008) and Chen *et al.* (2013) pointed out that for $Re = 0.05$ to 1.8×10^4, the pressure fluctuation was much higher for the downstream deck of the twin deck configuration. Therefore, the current study focused on capturing the flow patterns around the multi-box Megane deck section, for angles of attack $\alpha = -4°, -2°$ 0°, 2°, 4° at $Re = 9.3 \times 10^7$. From the vorticity contours, it was noticed that in general, the wind flow had a complex behavior, slipping through the gaps between the deck and shifting from upper deck to lower deck or vice-versa, depending on the angle of attack. For positive angles of attack the first two decks, A and B, acted as a single bluff body from which layers shed and re-attached onto the upper surface of the decks C and D; these combined with the flow raising upwards through the middle gap, especially for α = 0° and 2° (Figs. 7(a) and 7(b)) and shed downstream into the flow, from the downstream edge of the deck D. The turbulent flow has formed mostly underneath the middle decks B and C, for α = 0°, 2° and 4° (Figs. 7(a)-7(c)). For the negative angles of attack, α= -2° and -4°, the wind flow transited upwards through the last two gaps, thus the intensity of the reduced wind speed increasing on the upper surface of deck C; for the last deck D a separation bubble was noticed on the upper surface of the deck, caused by the flow detachment at the windward edge of deck, followed by a periodic flow re-attachment at the middle of deck D (Figs. 7(c) and (d)). The bluff-body behavior of the first two decks was not encountered for α = -2° and -4°, but intermittent shear layers detached from the corner of the deck B and traveled upwards into the flow, without re-attaching on the other decks.

The evolution of wind flow patterns for the upper and lower deck surfaces is shown in Figs. 8(a)-8(j). The main difference between the positive and negative angles of attack consisted in the presence of the wind flow formations along the edges (Figs. 8(a) and 8(e)) or almost enveloping the entire decks (Fig. 8(c)) for positive angles, while for negative angles of attack the flow became turbulent on the last two decks (Figs. 8(g) and 8(i)). Also, for negative angles of attack a sudden increase of the reduced wind speed was noticed on the upper surface of the deck D which indicates a flow separation. More important, a split-flow pattern was identified for α= -2° and 2° starting from the front edge of deck C (Figs. 8(c) and 8(g)). It is worth mentioning that a similar split-flow pattern was identified by smoke visualization during the wind tunnel tests performed for a modified Messina bridge multi- deck section by Belloli *et al.* (2013).

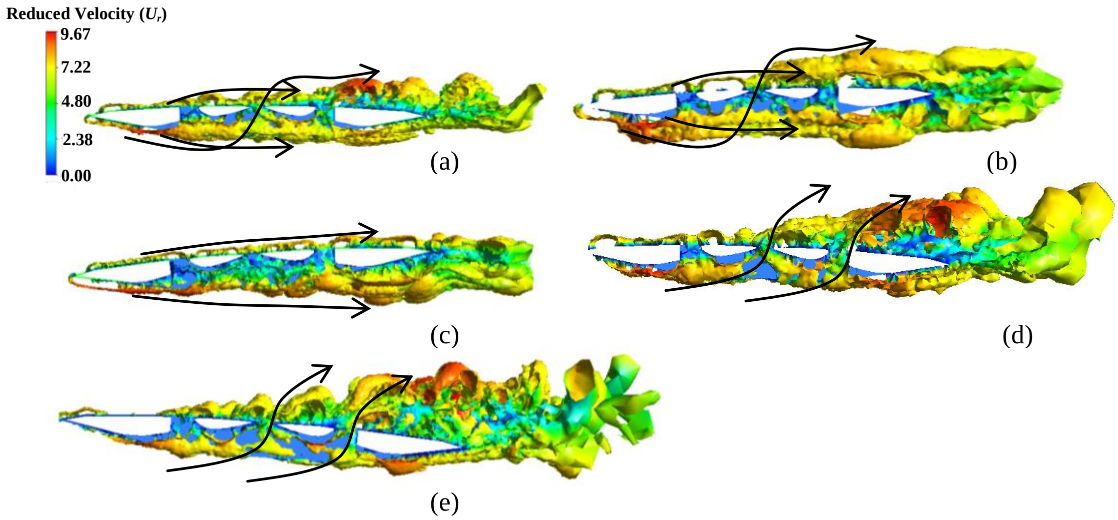

Fig. 7 Three-dimensional flow patterns around Megane multi-box deck for (a) α = 0°, (b) α = 2°, (c) α = 4°, (d) α = -2° and (e) α = -4°

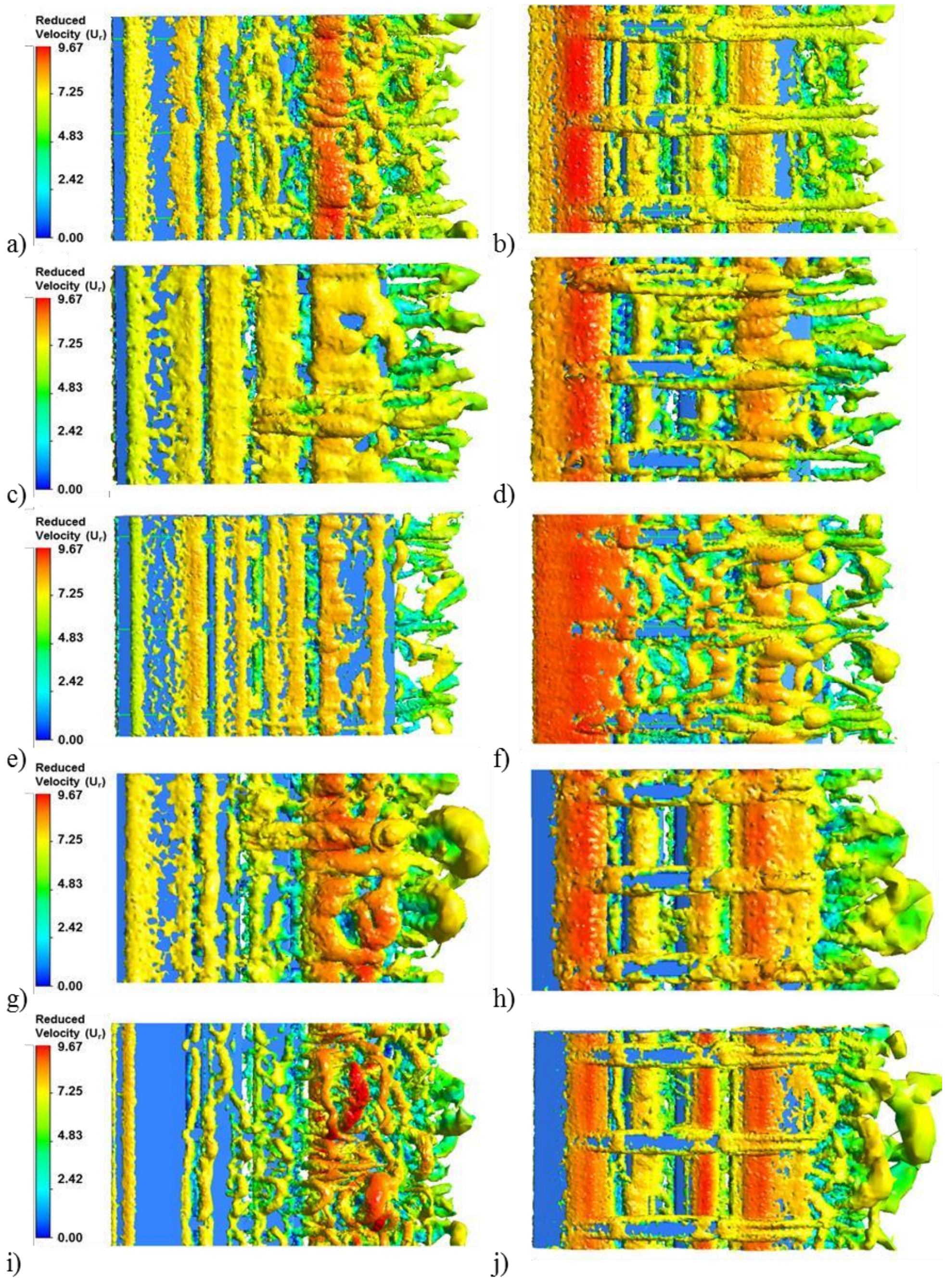

Fig. 8 Three-dimensional swirl plume around the Megane deck section for (a) a = 0°, upper deck, (b) a = 0°, lower deck, (c) a = 2°, upper deck, (d) a = 2°, lower deck, (e) a = 4°, upper deck, (f) a = 4°, lower deck, (g) a = -2°, upper deck, (h) a = -2°, lower deck, (i) a = -4°, upper deck, (j) a = -4°, lower deck

If on the upper deck, the generation of flow formations was controlled by the position and dimensions of the gaps, on the lower deck, the position of the connecting beams significantly influenced the flow patterns. The common feature for all the analyzed cases, α = -4°, -2°, 0°, 2°, and 4°, was the wind flow formed on both sides of each connecting beam, forming a longitudinal vortex trail towards the edge of the deck D, which is further shed upwards into the flow (Figs. 8 (b), 8(d), 8(f), 8(h) and 8(j)). For negative angles of attack the vortex trails combined with the flow incoming from the main body of the upper deck D forming swirly loops downstream the deck (Figs. 8 (h) and (j)). Overall, the three-dimensional flow patterns have indicated intense turbulent flow formations on the upper surface of the multi-box Megane deck section, thus a special consideration was given for the wind speed profiles at these locations.

4 Wind speed profile and pressure distribution for the Megane bridge deck section

In order to determine the effect of the connecting beams configuration on the formation of turbulent flow on the upper surface of the deck, the wind speed profiles at the middle of each deck was recorded, along the connecting beams and between two consecutive beams. In general, the high intensity wind speed profile is characterized by a sudden increase of wind speed within a short height. For α = 0° the 50 m/s wind speed (equivalent to the inlet wind speed) was reached in the first 1.0 m above the decks A, B and C, and no significant difference for the regions between the beams and along the beams was noticed; for the last traffic deck D however, the wind profile up to 0.8 m height was smoother for the area between the beams, followed by a sudden increase of up to U/U_{in} = 1.2 at around 1.5 m above the deck (Fig. 9(a)).

The wind speed increased the most, for the along beams region, for deck D, when compared with all the other locations, reaching up to 50 m/s at 0.8 m and almost 55 m/s at 1.5 m above the deck. Also on the deck D, for both cases, along and between the beams, the wind profile decreased very slowly with the height at a distance of 5.0 m still encountering very high values of 50 m/s. The evolution of the wind speed profiles for α= 2° was similar to the case of α= 0°, with a smoother wind speed profile for the region between the beams, and a steeper wind speed profile for the regions along the beams, on deck D; the wind speed profiles on the other decks, A, B and C, were very similar, for both, along and between the beams locations (Fig. 9(b)); the wind speed however did not register values higher than 48 m/s. Fig. 9(c) shows very consistent wind profiles for α = 4°, regardless the position where the measurements were taken, on the beams or between the beams. Wind speeds will increase in the immediate vicinity of the deck until approximately 40 m/s for the first decks A, about 48 m/s for decks B and C and up to 50 m/s for the last deck D. For the negative angles of attack, when the wind direction changes to upwards, thus flow passing through all three gaps and shedding turbulent flow formations were registered on the upper surfaces (Figs. 8(g) and 8(i)), the wind speeds at the middle of the decks A, B and C were around 45 m/s in the first 0.8 m from the deck for both investigated cases, along and between the connecting beams (Figs. 9(d) and 9(e), with the exception of the deck C, where a transitory wind speed profile was registered between the beams, with lower wind speed values of 32 m/s at 0.8 m and 41 m/s at 1.5 m height above the deck. On the last deck D, for along beams region, the wind speed reached almost 50 m/s in the first 0.8 m from the deck, however it increased with height and stabilized again from 4.0 m height onwards. For the region between the beams on the deck D, a similar transitory wind speed profile was noticed, with wind speeds much lower than expected of about 15 m/s at 0.8 m, 27 m/s at 1.5 m and 41 m/s at 2.15 m height.

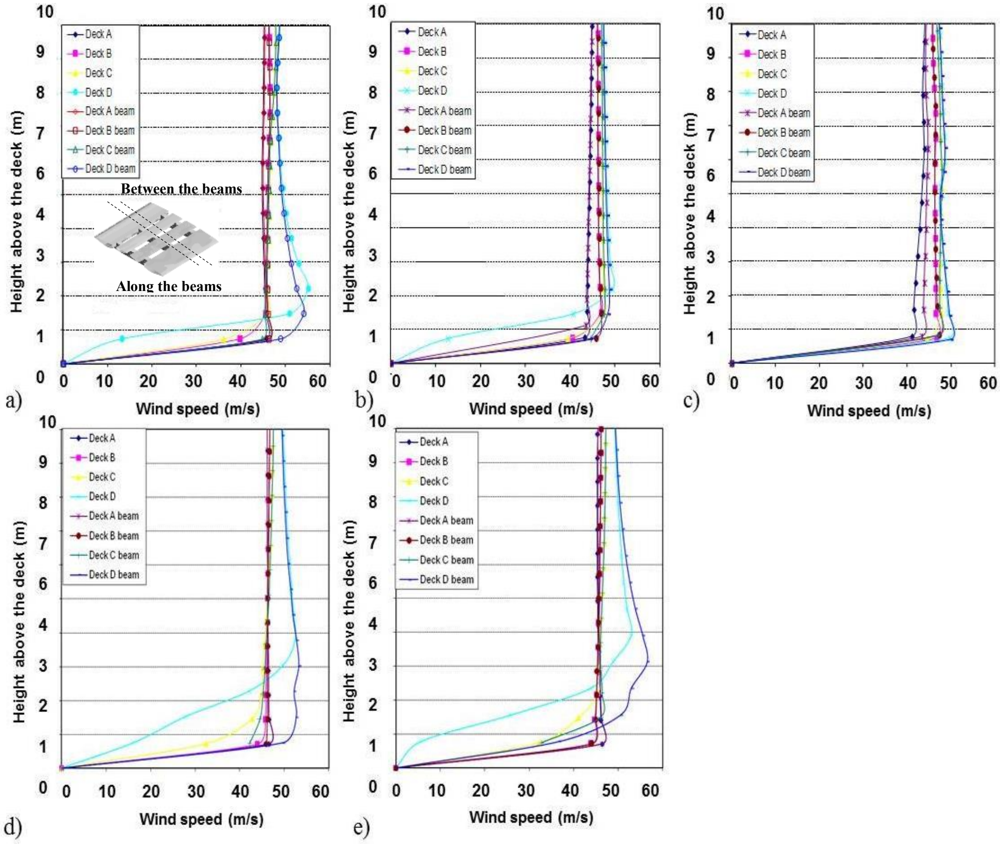

Fig. 9 Wind speed profiles at the middle of the decks for (a) α = 0°, (b) α = 2° , (c) α = 4°, (d) α = -2° and (e) α = -4°

For all the cases, the wind stabilized from a height of 2-3 m, towards a constant wind speed of about 45 m/s, which is the initial incoming wind speed. It is interesting to note that the wind speed will increase gradually with the position of the decks, deck A always registered the lowest speed and deck D always encountered the highest speeds; for some cases, even more than 10 m/s difference was registered between the first and the last decks (Fig. 9(c)), as detailed above; this indicates that the movement of the shear layers accelerated, and it generated turbulent flow formations mostly towards the end of the multi-box Megane deck section, as also represented in Figs. 8(a)-8(j).

Figs. 10 (a) and 10(b) represent the average pressure coefficients averaged along three rings on the front, middle and back decks and beams (Fig. 10(a)) and along two rings around the front and back deck section segments (Fig. 10(b)). For α= 0°, the pressure coefficients along the deck and the beams showed a positive pressure on the upwind edge of the deck A, of up to 1.0 which gradually decreased along the upper surface of the decks A, B and C, however a strong negative pressure, was noticed on the upper surface of the deck D, near the upwind edge, which indicates a flow detachment, corresponding to the increased wind speed region signaled in Fig. 8(a). Increasing the angle of attack to α = 2° and 4° has influenced the evolution of the pressure coefficient on the upper surface of the deck, which showed negative values for the traffic deck D and on the lower surface of the deck A (Fig. 9(a)).

Because of the sharp geometry of the corner, for α = -2° and -4° there was a negative pressure coefficient induced by the incoming flow impinging from underneath the deck but because of the flow re-attachment in the middle gap region a high pressure coefficient was noticed for the upper surface of the last two decks C and D.

The presence of the gaps between the decks has influenced the pressure coefficients and positive peaks caused by the flow re-attachment unto the upper surface at the edges for the decks A, B C and D for α= 0°, the decks A and D for α= 2° and the decks A, B and D for α= 4°. For the negative angles of attack, the flow direct impact on the lower surface determined positive pressure coefficient peaks for the upwind edges for the decks A and D for α= -2°, and for the decks A, B, C and D for α = -4°. The negative pressure peaks were caused by the detachment of the turbulent flow formations underneath the deck for the downwind edges for the decks A, B C and D for α = 0°, and for the decks A, C and D for α = 2° or by the flow separation for the upwind edges of the decks A, B and D for α= 4°. For the negative angles of attack, negative peaks in pressure coefficient were registered at the downwind edges of the decks A, B, C and D for α= -2° and the decks A and C for α= -4°. Therefore it was noted that the position of the connecting beams influenced the pressure coefficient by diminishing the negative or positive peaks, and ensured a smoother transition within the pressure variation along the decks for both upper and lower surface regions.

In order to determine the clarify the turbulent flows and vortices formations around the multi-box Megane bridge deck surface, especially at the locations where the pressure coefficients registered strong positive and negative peaks (Figs. 10(a) and 10(b)), the pressure contours for the flow field around the deck section were represented in Figs. 10(a)-10(e), for angles of attack, α = 0°, 2°, 4°, -2° and -4°; because the rings monitored along the deck and gaps (Fig. 10(b)) indicated more often positive peaks, then only the representation for the deck and between the gaps was considered.

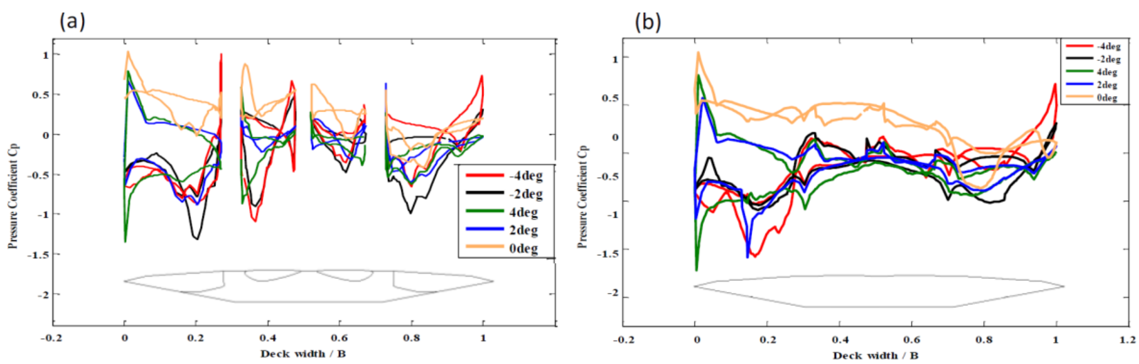

Fig. 10 Pressure coefficient distribution for Megane multi-box deck section for (a) Along beams and decks rings and (b) Along individual decks

The pressure contours were consistent with the pressure coefficient distribution represented in Figs. 8 and with the flow patterns described in Figs. 8 above. For α= 0°, when the first traffic decks A and the railway decks B and C, formed a bluff body, and continuous shear layers were shed towards the deck D, where the presence of a separation bubble with negative pressure was noticed at the upwind edge of deck D (Fig. 11(a)). For α= 2° and 4°, no major variations were noticed in the pressure field around the Megane deck section, except for the suction bubble created on the lower deck at the at the corner of the first deck A (Figs. 8(b) and 8(c)) which confirms the negative pressure coefficient peaks in Fig. 10(b). Also, for positive angles of attack, suction was registered underneath the decks A and D. For the negative angles of attack, α= -2° and -4°, clear vortices of negative pressure were noticed travelling along the traffic deck D, detaching around its middle region and shedding upwards into the flow (Figs. 11(d) and 11(e)); these are consistent with the flow patterns description in Figs. 8(a)-8(j), where longitudinal turbulent formations were reported, which now can be confirmed to be high speed vortices shedding.

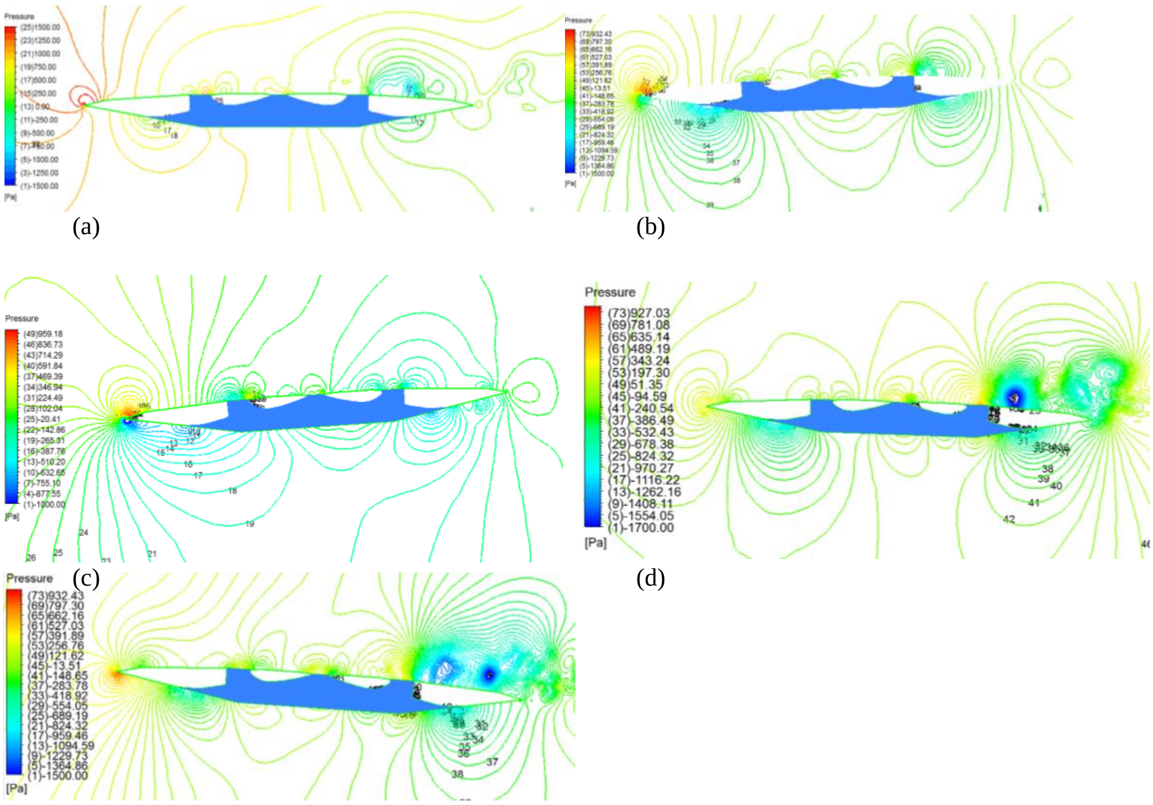

Fig. 11 Pressure isolines around the Megane multi-box deck section for (a) α = 0°, (b) α = 2°, (c) α = 4°, (d) α = -2° and (e) α = -4°

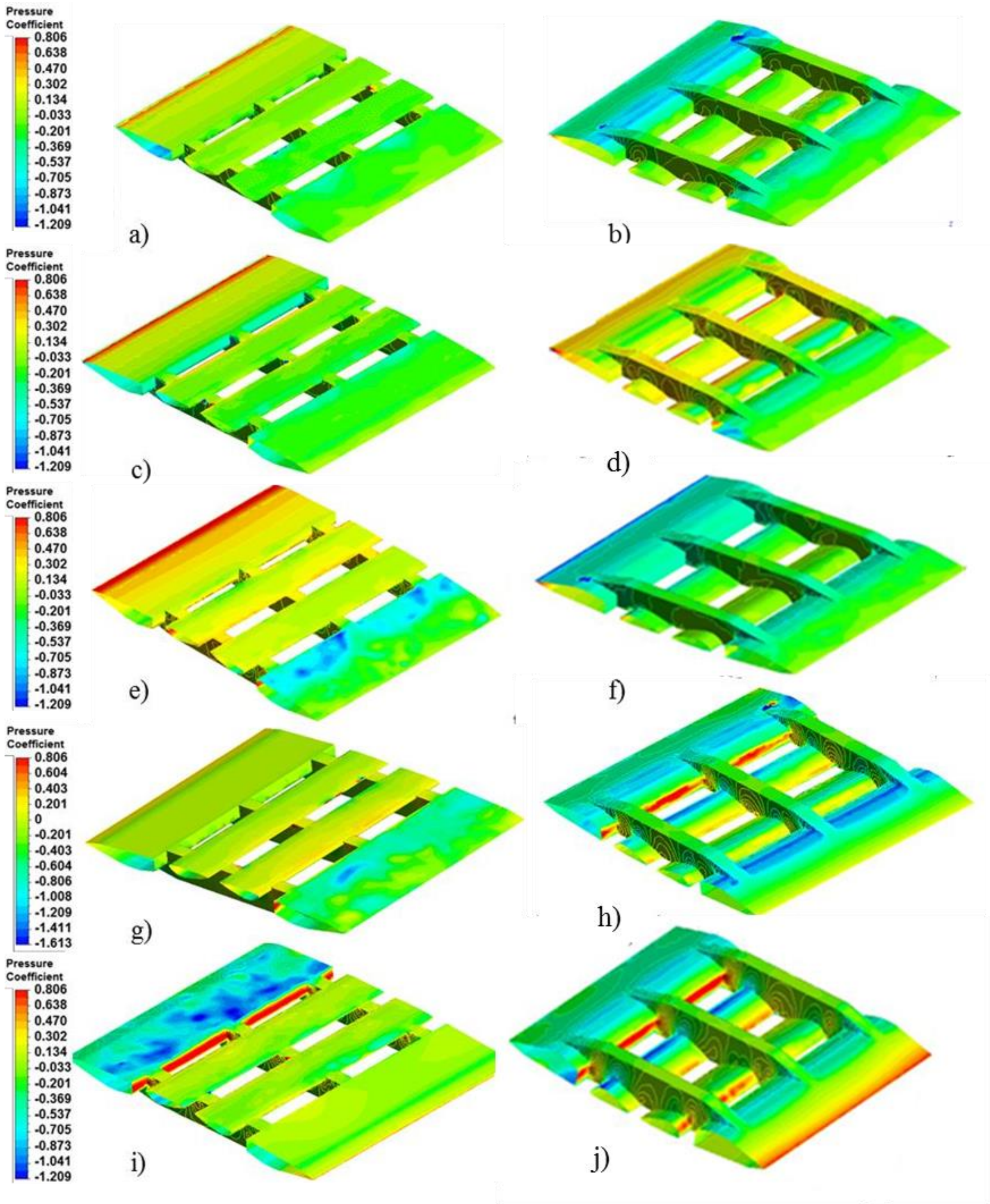

Fig. 12 Mean pressure coefficients distribution for Megane multi-box deck section (a) Cp_{UP} for α = 0° (b) Cp_{DOWN} for α = 0°, (c) Cp_{UP} for α = 2°, (d) Cp_{DOWN} for α = 2°, (e) Cp_{UP} for α = 4°, (f) Cp_{DOWN} for α = 4°, (g) Cp_{UP} for α = -2°, (h) Cp_{DOWN} for α = -2°, (i) Cp_{UP} for α = -4° and (j) Cp_{DOWN} for α = -4°

Figs. 12 (a)-12(j) represent the mean pressure coefficient on the upper and lower surfaces of the Megane bridge deck. For $\alpha = 0°$ a positive pressure on the upwind edge of deck A, of up to 0.7 was observed, which gradually decreased along the upper surface of decks A, B and C (Fig. 12(a)). Also, high negative pressure coefficients up to -1.2 were recorded on the upper surface of deck D, near the upwind edge. This negative pressure indicates the detachment of the wind flow, corresponding to the increased wind speed region. For $\alpha = 2°$, much smaller negative pressure coefficients were observed on the upper deck, of up to -0.5 for the traffic deck D and on the lower surface of deck A (Figs. 12(c) and 12(d)), while for $\alpha = 4°$ (Fig. 12(e)), the downward inclination of the deck caused the incoming flow to impact the upwind edge of deck A, where a high pressure coefficient of 0.8 is noticed. The flow detachment signaled by the high wind speed on the lower surface of deck A induced negative pressure coefficients of -1.2 distributed almost uniformly along the lower deck A, as it can be noticed in Fig. 12(f). Because of the sharp geometry of the corner, the pressure coefficient induced by the impinging incoming flow was lower than the previous cases, registering values of -0.5 for $\alpha = -2°$ (Fig. 11(g)). However the increased wind speed on the deck D, which was shown in Fig. 9(e), determined a flow re-attachment in the gap region, which induced very high pressure coefficients of up to 0.8 Pa, on the inner wall of the gap preceding the last deck D (Figs. 12(g) and 12(h)).

A strong suction can be noticed from the middle region of the lower surface of the deck A, which can be associated with the high wind speed observed in the same region in Fig. 12(h). Also, Figs. 12(g) and 12(h) show a distinct pressure coefficient distribution for $\alpha = -2°$ when compared with the other angles of attack. For the upper surface of the deck, especially for the first traffic deck A, suction of up to -1.6 towards the edge were registered, corresponding to a longitudinal vortex formation which detached from the surface in this region and shed upwards into the flow. Along the lower surfaces of the decks A and B, negative pressure coefficients of up to -1.2 were induced, while high positive pressure coefficients of up to 0.8 were recorded only along the downwind edge of the deck D, caused by the trail of turbulent formations visualized in Fig. 12(h).

5 Aerodynamic force coefficients for the Megane multi-box bridge deck section

5.1 Aerodynamic force coefficients from CFD-LES simulations

The drag lift and moment coefficients were determined separately for each of the decks and for the beams as represented in Figs. 13(a)-13(c). These coefficients were normalized with the widths of each deck segment as presented in Fig. 1 (namely 8.0 m for traffic decks A and D, 5.0 m for railway decks B and C and 2.5 m for beams) and with the entire deck width B, for the Megane multi-box deck. It was noticed that the two middle railway decks, B and C have encountered very similar distributions, namely, the drag coefficient C_D increased slightly for $\alpha = 4°$; The traffic decks A and D had almost opposite distribution for the drag coefficients, however with smaller values for A deck and very high drag of up to $C_D = 0.16$ at for $\alpha = 4°$, for the D deck (full lines in Fig. 13(a)). For the middle decks B and C, the lift coefficient increased up to $C_L = 0.1$ for the negative angles of attack, $\alpha = -2°$ and $-4°$ and decreased up to $C_L = -0.14$ for positive angles, $\alpha = 2°$ and $4°$ (interrupted lines in Fig. 13(b)). The lift coefficient for the deck D had a broad variation when compared with the other three decks, from $C_L = -0.6$ for $\alpha = -4°$, to $C_L = 0.24$ for $\alpha = 4°$ (full lines in Fig. 13(b)), which can be explained by the strong wind-induced suction and the vortices formed on the upper surface of the deck D, for negative angles of attack as described in

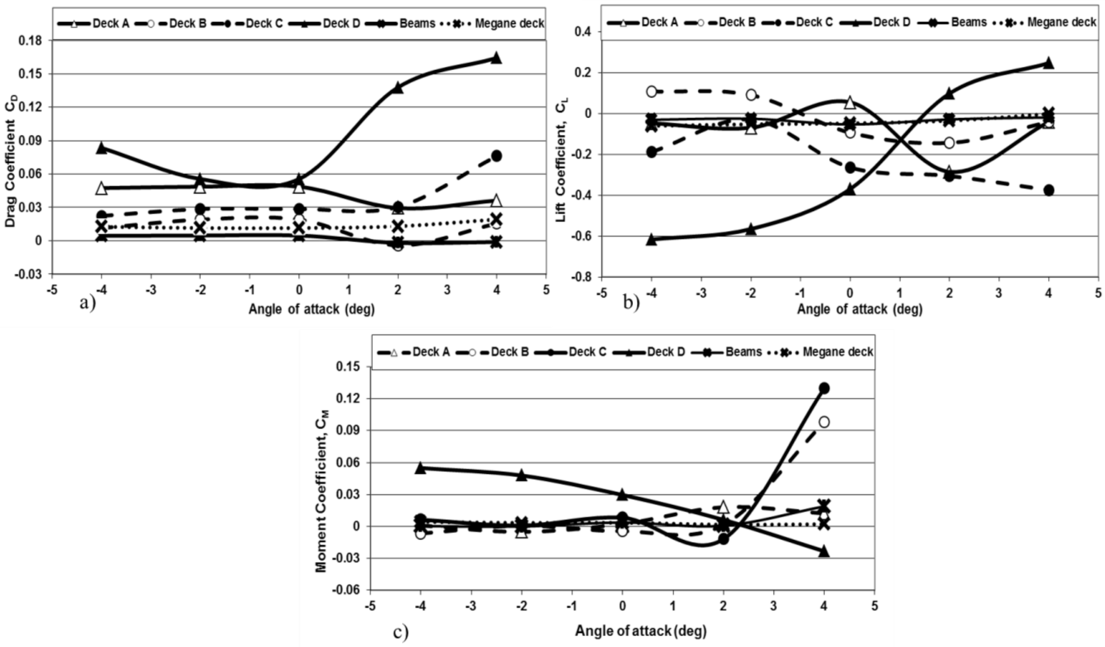

Fig. 13 Aerodynamic coefficients for the individual decks A, B, C, D and for the Megane multi-box bridge deck (a) drag coefficient, C_D (b) lift coefficient, C_L (c) moment coefficient, C_M

Figs. 9(d) and 9(e), phenomena which is not obvious for other angles of attack. The moment coefficient was almost negligible for the decks A, B and C, except for the α = 4°, where the moment will suddenly increase for the middle decks B and C (Fig. 13(c)). The last traffic deck D registered higher values of moment for negative angles of attack and decreased gradually for positive angles. It is interesting to note that the overall drag, lift and moment coefficients for the entire multi-box Megane bridge section, as well as for the connecting beams, maintained very low values of C_D = 0.01 to 0.02, C_L = -0.06 to -0.002 and C_M = 0.002 to 0.004, in spite of the variation recorded for some of the deck segments.

5.2 Experimntally obtained aerodynamic force coefficients

The bridge deck sectional model used in the experiment consisted by four individual airfoil shape decks connected by three beams with equal distances. The scale ratio for the model is 1:80 from the prototype shown in Fig. 1. The length of the sectional model is 1.00 m and the total width is 0.775 m (Fig. 14(a)). The bottom curvature of the cross-section was too complex to reproduce, therefore a 3-D printing technology was employed for the external shell of the model and for the connecting beams. The inside of the bridge deck model was filled with low density foam and four aircraft-graded aluminium strips with 4.0 mm thickness were attached on the top surface of all four individual decks to eliminate the roughness and also to increase the stiffness of the model. Two plywood and foam end plates were mounted on each of the extremities of the Megane bridge deck model. The bridge deck model under construction, with aluminium plates only on the traffic decks

A and D is shown in Fig. 14(a) and the finalized deck model installed in the wind tunnel test section is presented in Fig. 14(b). The tests were conducted in the open-circuit suction boundary layer wind tunnel with the test sections of 1.12 m height, 1.68 m width and 2.44 m length. The five-bladed fan has a diameter of 1.67 m and was powered by a 30 kW motor which can achieve wind speeds of up to 17 m/s. The turbulence intensity in the wind tunnel can range between 1.5% and up to 12% when surface roughness elements and spires are used.

Two aluminium bars extended out from the endplates of the Megane bridge deck model and were connected to a steel frame support system outside the wind tunnel testing section. The bridge deck model was fixed during the tests and two force balances were used to measure the forces induced by flow to the bridge section, for velocities up to 10 m/s and angles of attack ranging from -6° to 6°, varying every 2°. Static force coefficients C_L and C_D corresponding to measured lift and drag aerodynamic forces were determined from the experiment.

Similar trend and values were noticed for the experimentally obtained drag coefficients and the CFD-LES simulated drag coefficients of the Megane multi-box deck (Fig. 15(a)) ranging between 0.17 and 0.07 for the experiments, and between 0.12 and 0.07 for the CFD-LES simulations. The drag coefficients of the Megane model, scaled 1:80, yielded slightly higher values than the CFD-LES simulations, especially for -4°. The experimentally obtained lift coefficients for the Megane multi-box decks were smaller for the negative angles of attack, the biggest discrepancy being reported for -4°, where the experiments yielded CL = -0.07 while the CFD-LES simulation showed a value of CL = -0.027 (Fig. 15(b)); a better agreement was noticed with the decrease of the angle of attack, however for positive angles the lift coefficients obtained from experiments were higher than the CFD-LES results, reaching a values of 0.025 and 0.07 respectively, for 4°. Because the differences in lift coefficient diminish as the angles of attack approaches 0°, the differences registered for angles of attack of -4° and 4°, might be attributed to the difference of turbulence intensity around the bridge deck when the CFD-LES algorithm is employed. More advanced turbulent models such as Dynamic Smagorinsky model used in conjunction with more refined grid and computational domains might diminish this difference; however for the current investigation, due to the computer capacity limitations more refined meshes with more than 6 mil cells, failed to initiate, thus the coefficients reported in Fig. 15(b) were considered for the comparison with the experimental results.

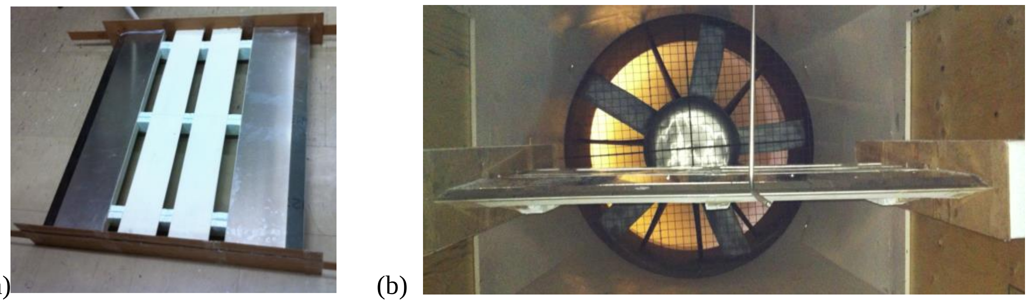

(a) (b)

Fig. 14 (a) Megane bridge deck model under construction and (b) Megane bridge deck model installed in the wind tunnel test section

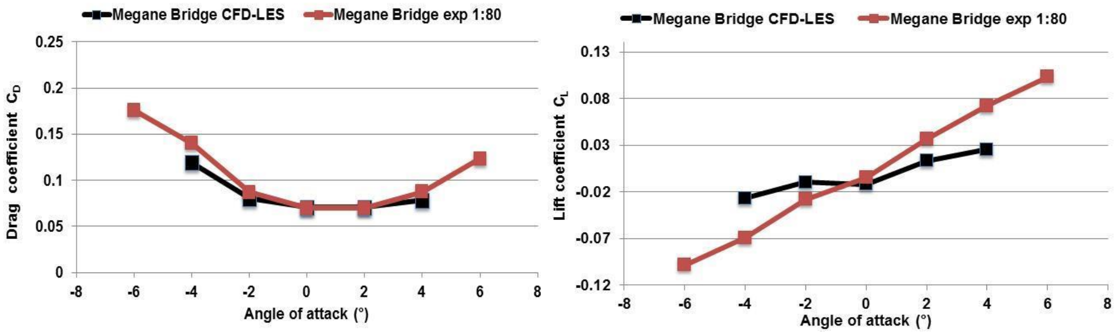

Fig. 15 Aerodynamic force coefficients comparison (a) drag coefficient, C_D (b) lift coefficient, C_L (c) moment coefficient, C_M

The geometry employed for the Megane multi-box deck has similarities with the geometry proposed for the Messina Bridge (Diana *et al*. 2008), which has two gaps and three box decks connected between them with lateral stabilizing beams of similar shape as the beams used in the current study. However, most of the studies reported for the Messina Bridge deck included the windshields, barriers, flaps, and other additional elements of the deck, thus a direct comparison could not be used in this study. Nevertheless it can be mentioned that the force coefficients reported for Messina Bridge deck showed good agreement between the CFD and the wind tunnel results however these did not overlap for all the angles of attack investigated showing some discrepancies for (Nieto *et al*. 2008). Also the CFD studies conducted by Larsen, 2008 who studied the vortex for twin decks, and Kuroda (1997) who studied the H4.1 and H9.1 compact box decks, showed that the aerodynamic force coefficients are in good agreement, but not identical, when CFD results were compared with the wind tunnel results. The moment coefficient for the Megane multi-box bridge deck was not measured in the current experiment, because only the two components force balance was used, therefore the torsion could not be measured.

6. Conclusions

An extensive three-dimensional LES-CFD analysis and a static wind tunnel experiment were performed for the 1:2 Megane multi-box bridge deck at $Re = 9.3 \times 10^7$ and for the 1:80 model of the Megane multi-box bridge deck section, for $Re = 5.1 \times 10^5$ respectively. Overall, the averaged aerodynamic coefficients for Megane multi-box deck section, had a good agreement, when compared with the results from the experiments performed for Messina bridge deck section (Diana *et al.*, 2008) and Xihoumen twin bridge deck section (Ge and Xiang 2009).

The aerodynamic lift coefficients determined through the wind tunnel experiment for the Megane deck, were slightly higher than those obtained from the CFD simulations for the negative angles of attack and lower than the experiments for the positive angles of attack. Also it was noticed that the individual traffic and railway decks behaved differently under the effect of wind flow, thus the aerodynamic forces coefficients registered variations from one individual deck to another, the most affected being the last traffic deck D. Thus the static aerodynamic forces measured in the wind tunnel experiment, for the entire model, cannot capture such variations for the Megane bridge deck, and in general for the multi-box bridge decks.

The three-dimensional LES-CFD investigation provided detailed information regarding the pressure and vorticity contours and offered a visual confirmation of the flow characteristics in the vicinity of the Megane multi-box deck. For most of the *Re* numbers and angles of attack analyzed in the current study, the traffic deck D has shown a tendency of generating longitudinal vortices and turbulent flow formations on both upper and lower surfaces of the deck, more significant for negative angles of attack, because of the flow coming upwards through the last gap between the decks C and D. A localized phenomenon occurred for $\alpha = 2°$ and $-2°$ when a longitudinal turbulent flow shedding from deck C towards deck D was noticed, only on one side of the Megane deck.

Also the wind speed profiles monitored on top of each of the decks, for the regions between two consecutive beams and along the beams showed that a gradual wind speed increase from deck A to the traffic deck D, which encountered the highest wind speeds, developed within a short height on top of the deck. The position of the connecting beams had the effect of diminishing these differences, especially for the pressure distribution at the surface of the deck. Also the pressure coefficients and the pressure distributions on the upper and lower surfaces of the deck, confirmed the flow patterns visually identified for the Megane multi-box bridge deck. Overall the multi-box Megane deck section is expected to achieve very good aerodynamic characteristics when the windshields and stabilizing flaps will be attached to the traffic decks A and D.

Acknowledgments

The authors would like to thank to Mr. Y. Tun for his valuable input regarding the meshing of the models and to Dr. J. Hayes and the technical staff from the boundary layer wind tunnel laboratory of Carleton University. The financial support provided by NSERC is also acknowledged.

References

American Society of Civil Engineers, (1986), *Manual of practice for wind tunnel testing of buildings and structures*, Reston, Virginia, USA.

Anderson, B., Anderson, R., Håkansson, L., Mortensen, M., Sudiyo, R. and van Wachem, B. (2011), *Computational Fluid Dynamics for Engineers*, Cambridge University Press, Cambridge, UK.

Anderson, J.D. (1995), *Computational Fluid Dynamics: The Basics with Applications*, McGraw-Hill Science, New York.

Belloli, M., Fossati, F., Giappino, S. and Muggiasca, S. (2013), "Vortex induced vibrations of a bridge deck: dynamic response and surface pressure distribution", *Proceedings of the 12th Americas Conference on Wind Engineering*, June, Seattle, USA.

Caracoglia, L. (2011), "Simulation of linear and non-linear propagation effects of a random turbulence field on bridge flutter instability", *J. Wind Eng. Ind. Aerod.*, **99**(9), 945-954.

Diana, G., Falco, M., Cheli F. and Cigada, A. (1999), *Experience gained in the Messina Bridge aerolastic project, long span bridges and aerodynamics*, Springer, Kobe, Japan.

Diana, G. Resta, F. and Rocchi, D. (2008), "A new numerical approach to reproduce bridge aerodynamic non-linearities in time domain", *J. Wind Eng. Ind. Aerod.*, **96**(10-11), 1871-1884.

Ge, Y.J. and Xiang, H.F. (2008), “Recent development of bridge aerodynamics in China”, *J. Wind Eng. Ind. Aerod.*, **96(**6-7), 736-768.

Ge, Y.J. and Xiang, H.F. (2008), “Bluff body aerodynamics application in challenging bridge span length”, *Proceedings of the VI BBAA*, Milano, July.

Ge, Y.J. and Xiang, H.F. (2009), “Aerodynamic stabilization for box-girder suspension bridges with super-long span”, *Proceedings of the 5th EACWE*, Florence, July.

Ge, Y.J., Yang, Y.X. and Cao, F.C. (2011), “VIV sectional model testing and field measurement of Xihoumen Suspension Bridge with twin box girder”, *Proceedings of the 13th International Conference on Wind Engineering*, Amsterdam, Netherlands, July.

Kwok, K.C.S., Qin, X.R., Fok, C.H. and Hitchcock, P.A. (2012), “Wind-induced pressures around a sectional twin-deck bridge model: Effects of gap-width on the aerodynamic forces and vortex shedding mechanisms”, *J. Wind Eng. Ind. Aerod*., **110**, 50-61.

Kuroda, S. (1997), “Numerical simulation of flow around box girder of a long span suspension bridge”, *J. Wind Eng. Ind. Aerod*., **67-68**, 239-252.

Larsen, A. and Walther J.H. (1997), “Aeroelastic analysis of bridge girder sections based on discrete vortex simulations”, *J. Wind Eng. Ind. Aerod*,, **67-68**, 253-265.

Larsen, A., Savage, M., Lafrenière, M., Hui, M. and Larsen, S.V. (2008), “Investigation of vortex response of a twin box bridge section at high and low Reynolds numbers”, *J. Wind Eng. Ind. Aerod*., **96**(6-7), 934-944.

Li, H., Laima, S., Ou, J., Zhao, X., Zhou, W., Yu,Y., Li, N. and Liu, N. (2011), “Investigation of vortex-induced vibration of a suspension bridge with two separated steel box girders based on field measurements”, *Eng. Struct*., **33**(6), 1894-1907.

Lin, T.Y. and Chow, P., (1991), “Gibraltar Strait Crossing, a challenge to bridge and structural engineering”, *IABSE J. Struct.Eng. Int*., **1**(2), 53-58.

Lee, S., Kwon, S.D. and Yoon, J. (2014), “Reynolds number sensitivity to aerodynamic forces of twin box bridge girder”, *J. Wind Eng. Ind. Aerod*., **127**, 59-68.

Mannini, C., Šoda, A., Voß, R. and Schewe, G. (2010), “Unsteady RANS simulations of flow around a bridge section”, *J. Wind Eng. Ind. Aerod*., **98**(12), 742-753.

Matsumoto, M., Mizuno, K., Okubo, K. and Ito, Y. (2007), “Flutter instability and recent development in stabilization of structures”, *J. Wind Eng. Ind. Aerod*., **95**(9-11), 888-907.

Matsuda, K., Cooper, K.R., Tanaka, H., Tokushige, M. and Iwasaki T. (2001), “An investigation of Reynolds number effects on the steady and unsteady aerodynamic forces on a 1:10 scale bridge deck section model”, *J. Wind Eng. Ind. Aerod*., **89**(7-8), 619-632.

Osborne, R. (1985), “On the Dynamical Theory of Incompressible Viscous Fluids and the Determination of the Criterion”, *Philos. T. R. Soc. London*, **186**, 123-164.

Ostenfeld, K.H. and Larsen, A. (1992), “Bridge Engineering and aerodynamics”, *Proceedings of the 1st Int. Symp. on Aerodynamics of Large Bridges*, A.A. Balkema Publishers, Denmark.

Park, K.H., Park, J.H., Lee, J.H., Seo, J.W., Yang, S.M., Kim, G.N., Lee, M.J. and Shin, S.K. (2009), “The planning and basic design of Ulsan Harbour Bridge”, *Proceedings of the Korea-China-Japan Symposium on Steel Structure Construction*, Seoul, November.

Schewe, G. and Larsen, A. (1998), “Reynolds number effects in the flow around a bluff bridge deck cross section”, *J. Wind Eng. Ind. Aerod*., **74-76**, 829-838.

Schewe, G. (2001), “Reynolds number effects in flow around a more-or-less bluff bodies”, *J. Wind Eng. Ind. Aerod.*, **89**, 1267-1289.

Simiu, E. and Scanlan, R.H., (1996), *Wind Effect on Structures*, John Wiley & Sons, Inc. New York, New York, U.S.A.

Shirai, S., and Ueda, T. (2003), “Aerodynamic simulation by CFD on flat box girder of super-long-span suspension bridge”, *J. Wind Eng. Ind. Aerod*., **91**, 279 - 290.

Smagorinsky, J. (1963), “General Circulation Experiments with the Primitive Equations”, *Mon. Weather Rev.* **91**(3), 99-164.

Wardlaw, R.L. (1992), “The improvement of aerodynamics performance”, *Proceedings of the 1st Int.Symp.*

on Aerodynamics of Large Bridges, A.A. Balkema Publishers, Denmark.
Xu, Y.L., Ko, J.M. and Yu, Z. (1997), “Modal analysis of tower-cable system of Tsing Ma long suspension bridge”, *Eng. Struct.*, **19**(10), 857-867.

AD